Direct radiative effects of airborne microplastics

Laura E. Revell[1,*], Peter Kuma[1,†], Eric C. Le Ru[2], Walter R. C. Somerville[2], Sally Gaw[1]

[1]School of Physical and Chemical Sciences, University of Canterbury, Christchurch 8140, New Zealand

[2]The MacDiarmid Institute for Advanced Materials and Nanotechnology, School of Chemical and Physical Sciences, Victoria University of Wellington, Wellington 6140, New Zealand

*Corresponding author, contact: laura.revell@canterbury.ac.nz

†Now at: Department of Meteorology, Stockholm University, Stockholm SE-106 91, Sweden

Microplastics are emerging as widespread contaminants in the atmosphere where, due to their small size and low density, they can be transported with winds around the Earth[1-25]. Atmospheric aerosols, such as mineral dust and other types of airborne particulate matter, influence Earth's climate by absorbing and scattering radiation (direct radiative effects). The impacts of aerosols on climate are commonly quantified with the effective radiative forcing (ERF) metric[26]. To date, the radiative effects of airborne microplastics and associated implications for global climate are unknown. Here we present the first calculations of the optical properties and direct radiative effects of airborne microplastics (excluding aerosol-cloud interactions). The ERF of airborne microplastics is computed to be 0.044±0.399 mW m^{-2} in the present-day atmosphere assuming a uniform surface concentration of 1 microplastic m^{-3} and a vertical distribution up to 10 km altitude. However, there are large uncertainties in the geographical and vertical distribution of microplastics. Assuming they are confined to the boundary layer, shortwave effects dominate and microplastic ERF is approximately -0.746±0.553 mW m^{-2}. Compared with the total ERF due to aerosol-radiation interactions[27] (-0.71 to -0.14 W m^{-2}), the microplastic ERF is small. However, plastic production has increased rapidly over the past 70 years[28]; without serious attempts to overhaul plastic production and waste-management practices, the abundance and ERF of airborne microplastics will increase in future.

Since large-scale production of plastics began in the 1950s, around 5 billion tonnes of plastic waste has accumulated in landfills or the environment to date[28]. Plastics become brittle as they age and may break down to produce microplastics and nanoplastics, typically defined as particles 1 – 5000 μm and <1 μm in size, respectively. Microplastics are ubiquitous pollutants in aquatic and terrestrial environments[29,30]. Primary sources of microplastics include pre-production pellets or nurdles used in the manufacture of plastic items and microbeads in personal care products, abrasive cleaning products, and paint and blasting abrasives. Secondary sources include synthetic fabric fibres, dust from synthetic rubber tyres, paint particles and the degradation of larger plastics that become brittle through exposure to UV radiation[25,31]. When inhaled in ambient air, micro- and nanoplastics may pose a threat to human health[32].

Measurements of airborne microplastics

In recent years airborne microplastics have been detected around the world (e.g. [1-23]). Common polymers detected in air include polyester, polyethylene, polypropylene, acrylic and resins (Extended Data Fig. 1). Airborne microplastics are typically collected by pumped air samplers, which yields a number concentration, or by collecting atmospheric fallout, yielding a deposition flux. Reported number concentrations of airborne microplastics to date are summarised in Fig. 1. Concentrations range between 0.01 microplastic (MP) m^{-3} (West

Pacific Ocean[15]) to 5650 MP m^{-3} (Beijing, China[13]). In contrast, total aerosol number concentrations over Europe and East Asia are typically on the order of $1 \times 10^9 - 1 \times 10^{10}$ m^{-3}, so microplastics are a relatively small component of total aerosol abundance[33]. It should be noted that no standardised procedure for sampling and analysing airborne microplastics currently exists, and comparing different studies must be done with caution. Nonetheless, measured concentrations of airborne microplastics vary by orders of magnitude depending on the sampling site, meteorological conditions and the analytical methods used.

The highest reported concentrations of microplastics to date (thousands of MP m^{-3}) were measured in London, UK[12], and Beijing, China[13]. These studies used Raman spectral imaging and Scanning Electron Microscopy – Energy Dispersive X-ray (SEM-EDX) spectroscopy, respectively, to detect airborne microplastics. In both studies, approximately half of the microplastics detected were between 5 – 10 μm in size. This size range is below the 11 μm detection limit of μFTIR spectroscopy, which was used in the majority of the other studies represented in Fig. 1. However, the high concentrations measured are also likely due to the locations of the sampling sites, which were urban sites in megacities. Reported concentrations of airborne microplastics are typically lower in remote environments compared with urban environments – for example, measurements[15] over the remote ocean have been reported on the order of 0.01 MP m^{-3}. Similarly, the concentration of microplastics measured on the French Atlantic coast in onshore winds was reported to be on average one-third of that measured in offshore winds[3].

Typically ranging between 15 – 250 μm in size (Extended Data Fig. 2, 3), airborne microplastics are one to two orders of magnitude larger than other types of atmospheric aerosols, which usually have diameters smaller than 2.5 μm. However, their low density (between 0.86 g cm^{-3} for polyethylene to 1.38 g cm^{-3} for polyethylene terephthalate and polyvinyl chloride, Extended Data Fig. 1) means they are easily entrained[34] and transported over large distances[24]. Given their hydrophobicity, they may be less likely to be deposited via cloud formation and precipitation compared with airborne particles of a similar size. Similar deposition fluxes of airborne microplastics were recorded in central Paris[7] and a remote mountain catchment in the French Pyrenees, far from any major population centre[2]. Modelling shows that microplastics generated from road traffic (tire wear particles and brake wear particles) have high transport efficiencies to remote regions[25]. It has furthermore been suggested that such particles may contribute to warming of the cryosphere due to their light-absorbing properties[25].

Atmospheric aerosols scatter and absorb solar and terrestrial radiation[26], leading to atmospheric warming or cooling depending on particle size, shape, composition and atmospheric and surface conditions. Overall, direct aerosol-radiation interactions have a negative effective radiative forcing (ERF; i.e. a cooling influence on surface climate); however, black carbon aerosol has a positive ERF and causes warming because it is highly absorbing of solar radiation[26]. Here we present the first approximation of the direct global radiative effects of airborne microplastics. We calculated the optical properties of non-pigmented fragments and fibres, the two most common microplastic shapes (Extended Data Fig. 4), and implemented the optical properties into a general circulation model (GCM) to calculate the ERF of airborne microplastics (see Methods).

Microplastic optical properties and ERF

The scattering cross sections of non-pigmented microplastic fragments and fibres (Fig. 2) indicate that microplastics are efficient at scattering ultraviolet (UV) and visible radiation which by itself would have a cooling influence on surface climate. However, the absorption cross sections indicate that microplastics absorb infrared radiation, including in the "atmospheric window" between 8 – 12 μm where few other species absorb in Earth's atmosphere. Microplastics may therefore contribute to the greenhouse effect. Overall, microplastics are predominantly scattering in the UV and visible regions as indicated by the single scattering albedo (Fig. 2) while in the infrared they absorb radiation almost as much as they scatter it.

GCM simulations performed with approximately the median microplastic concentration from Fig. 1 (1 MP m^{-3} uniformly distributed at the surface globally, with vertical scaling applied; see Methods) did not yield a clear signal-to-noise ratio in ERF in a 20-year simulation. Instead, simulations were performed assuming 100 MP m^{-3} at the surface, which is on the same order of magnitude as the mean concentration from Fig. 1 of 638 MP m^{-3}. The resulting ERF values are shown in Fig. 3a, and compared with the radiative forcing (RF) of common aerosol components as reported in the Intergovernmental Panel on Climate Change's Fifth Assessment Report (IPCC AR5)[26].

Non-pigmented microplastic fragments and fibres simulated with a near-surface concentration of 100 MP m^{-3} exert a longwave ERF of +0.164±0.086 and +0.229±0.110 W m^{-2}, respectively (Fig. 3b). Fragments and fibres exert a shortwave ERF of -0.183±0.088 and -0.268±0.066 W m^{-2}, respectively. Both findings are consistent with the absorption and scattering cross sections presented in Fig. 2. Since microplastics are large compared to other anthropogenic or natural aerosol particles, their effect on longwave radiation relative to their effect on shortwave radiation is expected to be larger than for other types of aerosol. Therefore, the longwave and shortwave effects almost cancel when microplastics are assumed to be present up to 10 km altitude. Overall, fibres have a larger influence on shortwave and longwave ERF than fragments because fibres tend to be larger (Extended Data Fig. 2, 3). The net ERF in a combined simulation assuming 50 fragments m^{-3} and 50 fibres m^{-3} is 0.004±0.040 W m^{-2} (i.e. between -0.036 and +0.044 W m^{-2}). This result is similar in magnitude to the RF of secondary organic aerosol (-0.03 W m^{-2} in IPCC AR5[26], however noting that secondary organic aerosol is the smallest forcing term of all aerosols considered by IPCC, and that its ERF has more recently been estimated[35] to span a wide range from -0.01 to -0.78 W m^{-2}).

The uncertainty in the sign of the microplastic ERF arises from the shortwave and longwave RFs having a similar magnitude for non-pigmented microplastics. Although 100 MP m^{-3} is a large surface concentration to prescribe globally, it is far below the highest concentration of airborne microplastics reported to date (Fig. 1). We selected 100 MP m^{-3} so as to separate signal from noise, as discussed earlier. Assuming that ERF scales linearly with concentration, microplastics in the combined fragments and fibres simulation yield a net ERF of 0.044±0.399 mW m^{-2} when the global-mean surface concentration is 1 MP m^{-3}; approximately the median concentration from Fig. 1. Thus, the computed microplastic ERF for the present-day atmosphere is small compared with the total aerosol ERF[27] of between -0.71 and -0.14 W m^{-2}.

So far only one study to date has identified the presence of microplastics above the planetary boundary layer, with concentrations ranging between 13.9 MP m^{-3} above urban areas and 1.5 MP m^{-3} above rural areas, at altitudes up to 3.5 km above sea level[36]. Understanding the vertical distribution of microplastics is important as it influences radiative fluxes[37]. A sensitivity simulation with microplastics confined to the lowest 2 km of the GCM yields a net ERF of -0.746±0.553 mW m^{-2} assuming a surface concentration of 1 MP m^{-3}. As can be seen in Fig. 3b, the longwave ERF is particularly sensitive to the vertical distribution of microplastics, as expected due to the decrease in temperature, pressure and water vapour with altitude. The longwave ERF becomes disproportionately smaller when microplastics span 0 – 2 km altitude rather than 0 – 10 km, yielding a pronounced net negative ERF. While the net ERF in the boundary layer experiment is still small compared to total aerosol ERF, it demonstrates that if airborne microplastics are present only in the boundary layer, then they will have a more significant impact on surface climate than if they are distributed throughout the troposphere.

Finally, Single Column Model (SCM) simulations were performed for selected geographical sites and solar zenith angles (see Methods) to investigate how much of the microplastic ERF is due to radiative effects versus rapid adjustments (for example, changes in clouds[38]). From SCM simulations with microplastics prescribed up to 10 km (with a surface concentration of 100 MP m^{-3} and vertical scaling applied, as in the GCM simulations), the mean RF was calculated over seven sets of atmospheric conditions (see Methods) with fixed cloud and temperature profiles. The mean RF is -0.016±0.089, -0.029±0.135, -0.040±0.123 and -0.032±0.024 W m^{-2} for

the fragments, fibres, combined and boundary layer simulations, respectively (Fig. 3b). In comparison, the global-mean ERF, calculated from the GCM and allowing all physical variables in the atmosphere to respond to microplastics, is -0.018±0.125, -0.039±0.104, 0.004±0.078 and -0.075±0.111 W m^{-2} for the fragments, fibres, combined and boundary layer simulations, respectively. Because the SCM was only run for seven specific cases, the results are not definitive; however the GCM-calculated ERF and SCM-calculated RF are similar in magnitude and direction, which suggests that the microplastic ERF is not obscured by or dominated by rapid adjustments. Running the SCM for all solar zenith angles, latitudes and longitudes would allow a thorough investigation into the contribution of rapid adjustments to the total microplastic ERF and should be addressed in future studies.

Discussion and outlook

Further research is needed to constrain our estimate of microplastic ERF. Firstly, more field studies across a range of urban and remote locations are needed to better understand the concentration of airborne microplastics – both in terms of the geographical and vertical distributions. The majority of the studies used to inform our estimate of microplastic surface concentration were carried out in Europe and Asia (Fig. 1). Other types of anthropogenic aerosol, such as nitrate aerosol, tend to exhibit peak concentrations over Europe and East Asia[39] and thus the studies considered here may not reflect the global average accurately. On the other hand, many studies to date used μFTIR spectroscopy, which cannot identify particles smaller than 11 μm. Particles in the 5-10 μm size range accounted for half the microplastics present in studies using SEM-EDX[13] and Raman spectral imaging[12]. Due to detection limits these studies were not able to indicate whether nanoplastics were present, however mass-based analysis methods suggest that they are[18]. Therefore along with more studies being performed around the world, analytical methods must be improved and standardised such that we can measure airborne plastics accurately.

As already discussed, the microplastic ERF is highly sensitive to the vertical distribution of microplastics because longwave radiative effects depend on aerosol size, along with atmospheric conditions such as temperature. Future studies identifying whether microplastics are distributed throughout the troposphere are thus essential for constraining microplastic ERF.

The optical properties of microplastics calculated in this study were based on refractive indices of pure polymers (Extended Data Fig. 5), which were the only wavelength-dependent data available (see Methods). In reality, environmental microplastics have a wide range of colours – commonly black, grey and red (Extended Data Fig. 6). The colouring is typically achieved by mixing pure polymers with organic or inorganic pigments, which alter the colour of the polymer via their effect on the complex refractive index in the visible spectrum. Similarly, it is expected that they also change the refractive index of the material in the infrared spectrum. Therefore, plastics composed of the same polymer will have variable refractive indices depending on the pigment and other potential additives found in the material, such as optical brighteners[40], along with any organic coatings they may have accumulated in the environment. It may be that pigmented microplastics are more absorbing than they are scattering in the visible spectrum, yield a net positive ERF, and contribute to atmospheric warming, as previously suggested[25]. Further research is needed to assess the range of possible refractive indices when pigments are bound in polymers, and the resulting range of microplastic ERF.

In calculating microplastic ERF, we considered only direct microplastic-radiation interactions. Atmospheric aerosols can influence cloud lifetime and albedo by acting as cloud condensation nuclei or ice nucleating particles[41,42]. Recent research indicates that nanoplastics are present in the atmosphere[18], and given their size range, may interact with clouds. Laboratory evidence suggests that, due to their hydrophobic nature, micro- and nanoplastics may act as cloud ice nuclei[43], however their contribution to cloud formation may depend on organic coatings accumulated in the environment and very little is known about this to date. Microplastic-cloud interactions may therefore be important too, especially in regions such as the Southern Ocean where clouds are

highly sensitive to the concentration of ice nucleating particles[44]. Limited evidence to date suggests that microplastic concentrations over the remote ocean are low[15], however microplastics are abundant in the world's oceans[45] and may be co-emitted with sea spray[3]. Moreover, recent modelling suggests that continents receive more microplastics from mismanaged plastic waste in the oceans (via co-emission with sea spray and atmospheric transport) than they produce in a year[24].

In summary, we calculate the ERF of non-pigmented airborne microplastics to be 0.044± 0.399 mW m^{-2} assuming a global-mean surface concentration of 1 MP m^{-3} and present throughout the troposphere, or -0.746±0.554 mW m^{-2} when confined to the atmospheric boundary layer. Uncertainties arise due to a current lack of data; the magnitude of ERF is influenced by the concentration of microplastics, and the sign is subject to uncertainties in the wavelength-dependent refractive index, which depends on properties such as composition and colour. Airborne microplastic pollution will become more severe in future; not only are microplastics durable but, based on current production and waste management trends, the abundance of plastic accumulated in landfills and the environment is projected to double over the next three decades[28]. Since plastic degrades through age and exposure to UV light to produce secondary microplastics, we expect microplastics to be present in Earth's atmosphere for many years to come. In the absence of serious efforts to address microplastic pollution, mis-managed plastic waste could exert an influence on climate in the future. Future research should assess whether microplastics influence climate regionally; anthropogenic aerosols have been linked to changes in heat extremes[46], and microplastics may similarly influence local and regional climate. This is especially true of urban environments, where airborne microplastics are already present on the order of hundreds to thousands of MP m^{-3}, and may already contribute locally to atmospheric heating and/or cooling.

References

1 Akhbarizadeh, R. *et al.* Suspended fine particulate matter (PM2.5), microplastics (MPs), and polycyclic aromatic hydrocarbons (PAHs) in air: Their possible relationships and health implications. *Environmental Research* **192**, 110339, doi:10.1016/j.envres.2020.110339 (2021).

2 Allen, S. *et al.* Atmospheric transport and deposition of microplastics in a remote mountain catchment. *Nature Geoscience* **12**, 339-344, doi:10.1038/s41561-019-0335-5 (2019).

3 Allen, S. *et al.* Examination of the ocean as a source for atmospheric microplastics. *PLOS ONE* **15**, e0232746, doi:10.1371/journal.pone.0232746 (2020).

4 Bergmann, M. *et al.* White and wonderful? Microplastics prevail in snow from the Alps to the Arctic. *Science Advances* **5**, eaax1157, doi:10.1126/sciadv.aax1157 (2019).

5 Brahney, J., Hallerud, M., Heim, E., Hahnenberger, M. & Sukumaran, S. Plastic rain in protected areas of the United States. *Science* **368**, 1257-1260, doi:10.1126/science.aaz5819 (2020).

6 Cai, L. *et al.* Characteristic of microplastics in the atmospheric fallout from Dongguan city, China: preliminary research and first evidence. *Environmental Science and Pollution Research* **24**, 24928-24935, doi:10.1007/s11356-017-0116-x (2017).

7 Dris, R., Gasperi, J., Saad, M., Mirande, C. & Tassin, B. Synthetic fibers in atmospheric fallout: A source of microplastics in the environment? *Marine Pollution Bulletin* **104**, 290-293, doi:10.1016/j.marpolbul.2016.01.006 (2016).

8 Dris, R. *et al.* A first overview of textile fibers, including microplastics, in indoor and outdoor environments. *Environmental Pollution* **221**, 453-458, doi:10.1016/j.envpol.2016.12.013 (2017).

9 Gaston, E., Woo, M., Steele, C., Sukumaran, S. & Anderson, S. Microplastics Differ Between Indoor and Outdoor Air Masses: Insights from Multiple Microscopy Methodologies. *Applied Spectroscopy* **74**, 1079-1098, doi:10.1177/0003702820920652 (2020).

10 Klein, M. & Fischer, E. K. Microplastic abundance in atmospheric deposition within the Metropolitan area of Hamburg, Germany. *Science of The Total Environment* **685**, 96-103, doi:10.1016/j.scitotenv.2019.05.405 (2019).

11 Knobloch, E. *et al.* Comparison of Deposition Sampling Methods to Collect Airborne Microplastics in Christchurch, New Zealand. *Water, Air, & Soil Pollution* **232**, 133, doi:10.1007/s11270-021-05080-9 (2021).

12 Levermore, J. M., Smith, T. E. L., Kelly, F. J. & Wright, S. L. Detection of Microplastics in Ambient Particulate Matter Using Raman Spectral Imaging and Chemometric Analysis. *Analytical Chemistry* **92**, 8732-8740, doi:10.1021/acs.analchem.9b05445 (2020).

13 Li, Y. *et al.* Airborne fiber particles: Types, size and concentration observed in Beijing. *Science of The Total Environment* **705**, 135967, doi:10.1016/j.scitotenv.2019.135967 (2020).

14 Liu, K. *et al.* Source and potential risk assessment of suspended atmospheric microplastics in Shanghai. *Science of The Total Environment* **675**, 462-471, doi:10.1016/j.scitotenv.2019.04.110 (2019).

15 Liu, K. *et al.* Consistent Transport of Terrestrial Microplastics to the Ocean through Atmosphere. *Environmental Science & Technology* **53**, 10612-10619, doi:10.1021/acs.est.9b03427 (2019).

16 Liu, C. *et al.* Widespread distribution of PET and PC microplastics in dust in urban China and their estimated human exposure. *Environment International* **128**, 116-124, doi:10.1016/j.envint.2019.04.024 (2019).

17 Liu, K. *et al.* Global inventory of atmospheric fibrous microplastics input into the ocean: An implication from the indoor origin. *Journal of Hazardous Materials* **400**, 123223, doi:10.1016/j.jhazmat.2020.123223 (2020).

18 Materić, D. *et al.* Micro- and Nanoplastics in Alpine Snow: A New Method for Chemical Identification and (Semi)Quantification in the Nanogram Range. *Environmental Science & Technology* **54**, 2353-2359, doi:10.1021/acs.est.9b07540 (2020).

19 Su, L., Nan, B., Craig, N. J. & Pettigrove, V. Temporal and spatial variations of microplastics in roadside dust from rural and urban Victoria, Australia: Implications for diffuse pollution. *Chemosphere* **252**, 126567, doi:10.1016/j.chemosphere.2020.126567 (2020).

20 Syafei, A. D., Nurasrin, N. R., Assomadi, A. F. & Boedisantoso, R. Microplastic Pollution in the Ambient Air of Surabaya, Indonesia. *Current World Environment* **61**, 290-298, doi:10.12944/cwe.14.2.13.

21 Wang, X. *et al.* Atmospheric microplastic over the South China Sea and East Indian Ocean: abundance, distribution and source. *Journal of Hazardous Materials* **389**, 121846, doi:10.1016/j.jhazmat.2019.121846 (2020).

22 Wright, S. L., Ulke, J., Font, A., Chan, K. L. A. & Kelly, F. J. Atmospheric microplastic deposition in an urban environment and an evaluation of transport. *Environment International* **136**, 105411, doi:10.1016/j.envint.2019.105411 (2020).

23 Zhang, Y. *et al.* Microplastics in glaciers of the Tibetan Plateau: Evidence for the long-range transport of microplastics. *Science of The Total Environment* **758**, 143634, doi:10.1016/j.scitotenv.2020.143634 (2021).

24 Brahney, J. *et al.* Constraining the atmospheric limb of the plastic cycle. *Proceedings of the National Academy of Sciences* **118**, e2020719118, doi:10.1073/pnas.2020719118 (2021).

25 Evangeliou, N. *et al.* Atmospheric transport is a major pathway of microplastics to remote regions. *Nature Communications* **11**, 3381, doi:10.1038/s41467-020-17201-9 (2020).

26 Myhre, G. *et al.* Anthropogenic and Natural Radiative Forcing. In: Climate Change 2013: The Physical Science Basis. Contribution of Working Group I to the Fifth Assessment Report of the Intergovernmental Panel on Climate Change. (Cambridge, United Kingdom and New York, NY, USA, 2013).

27 Bellouin, N. *et al.* Bounding Global Aerosol Radiative Forcing of Climate Change. *Reviews of Geophysics* **58**, e2019RG000660, doi:10.1029/2019RG000660 (2020).

28 Geyer, R., Jambeck, J. R. & Law, K. L. Production, use, and fate of all plastics ever made. *Science Advances* **3**, e1700782, doi:10.1126/sciadv.1700782 (2017).

29 Andrady, A. L. Microplastics in the marine environment. *Marine Pollution Bulletin* **62**, 1596-1605, doi:10.1016/j.marpolbul.2011.05.030 (2011).

30 de Souza Machado, A. A., Kloas, W., Zarfl, C., Hempel, S. & Rillig, M. C. Microplastics as an emerging threat to terrestrial ecosystems. *Global Change Biology* **24**, 1405-1416, doi:10.1111/gcb.14020 (2018).

31 Rochman, C. M. Microplastics research—from sink to source. *Science* **360**, 28-29, doi:10.1126/science.aar7734 (2018).

32 Goodman, K. E., Hare, J. T., Khamis, Z. I., Hua, T. & Sang, Q.-X. A. Exposure of Human Lung Cells to Polystyrene Microplastics Significantly Retards Cell Proliferation and Triggers Morphological Changes. *Chemical Research in Toxicology*, doi:10.1021/acs.chemrestox.0c00486 (2021).

33 Spracklen, D. V. *et al.* Explaining global surface aerosol number concentrations in terms of primary emissions and particle formation. *Atmos. Chem. Phys.* **10**, 4775-4793, doi:10.5194/acp-10-4775-2010 (2010).

34 Bullard, J. E., Ockelford, A., O'Brien, P. & McKenna Neuman, C. Preferential transport of microplastics by wind. *Atmospheric Environment* **245**, 118038, doi:10.1016/j.atmosenv.2020.118038 (2021).

35 Tsigaridis, K. & Kanakidou, M. The Present and Future of Secondary Organic Aerosol Direct Forcing on Climate. *Current Climate Change Reports* **4**, 84-98, doi:10.1007/s40641-018-0092-3 (2018).

36 González-Pleiter, M. *et al.* Occurrence and transport of microplastics sampled within and above the planetary boundary layer. *Science of The Total Environment*, 143213, doi:10.1016/j.scitotenv.2020.143213 (2020).

37 Mishra, A. K., Koren, I. & Rudich, Y. Effect of aerosol vertical distribution on aerosol-radiation interaction: A theoretical prospect. *Heliyon* **1**, e00036, doi:10.1016/j.heliyon.2015.e00036 (2015).

38 Lohmann, U. *et al.* Total aerosol effect: radiative forcing or radiative flux perturbation? *Atmos. Chem. Phys.* **10**, 3235-3246, doi:10.5194/acp-10-3235-2010 (2010).

39 Bellouin, N. *et al.* Aerosol forcing in the Climate Model Intercomparison Project (CMIP5) simulations by HadGEM2-ES and the role of ammonium nitrate. *Journal of Geophysical Research: Atmospheres* **116**, doi:10.1029/2011JD016074 (2011).

40 Optical brighteners: Improving the colour of plastics. *Plastics, Additives and Compounding* **5**, 42-46, doi:10.1016/S1464-391X(03)00049-7 (2003).

41 Twomey, S. The Influence of Pollution on the Shortwave Albedo of Clouds. *Journal of the Atmospheric Sciences* **34**, 1149-1152, doi:10.1175/1520-0469(1977)034<1149:tiopot>2.0.co;2 (1977).

42 Albrecht, B. A. Aerosols, Cloud Microphysics, and Fractional Cloudiness. *Science* **245**, 1227-1230, doi:10.1126/science.245.4923.1227 (1989).

43 Ganguly, M. & Ariya, P. A. Ice Nucleation of Model Nanoplastics and Microplastics: A Novel Synthetic Protocol and the Influence of Particle Capping at Diverse Atmospheric Environments. *ACS Earth and Space Chemistry* **3**, 1729-1739, doi:10.1021/acsearthspacechem.9b00132 (2019).

44 Vergara-Temprado, J. *et al.* Strong control of Southern Ocean cloud reflectivity by ice-nucleating particles. *Proceedings of the National Academy of Sciences* **115**, 2687-2692, doi:10.1073/pnas.1721627115 (2018).

45 Eriksen, M. *et al.* Plastic Pollution in the World's Oceans: More than 5 Trillion Plastic Pieces Weighing over 250,000 Tons Afloat at Sea. *PLoS ONE* **9**, e111913, doi:10.1371/journal.pone.0111913 (2014).

46 Boé, J., Somot, S., Corre, L. & Nabat, P. Large discrepancies in summer climate change over Europe as projected by global and regional climate models: causes and consequences. *Climate Dynamics* **54**, 2981-3002, doi:10.1007/s00382-020-05153-1 (2020).

47 Wessel, P. & Smith, W. H. F., A Global Self-consistent, Hierarchical, High-resolution Shoreline Database. *Journal of Geophysical Research: Solid Earth* **101**, 8741-8743, doi: 10.1029/96JB00104 (1996).

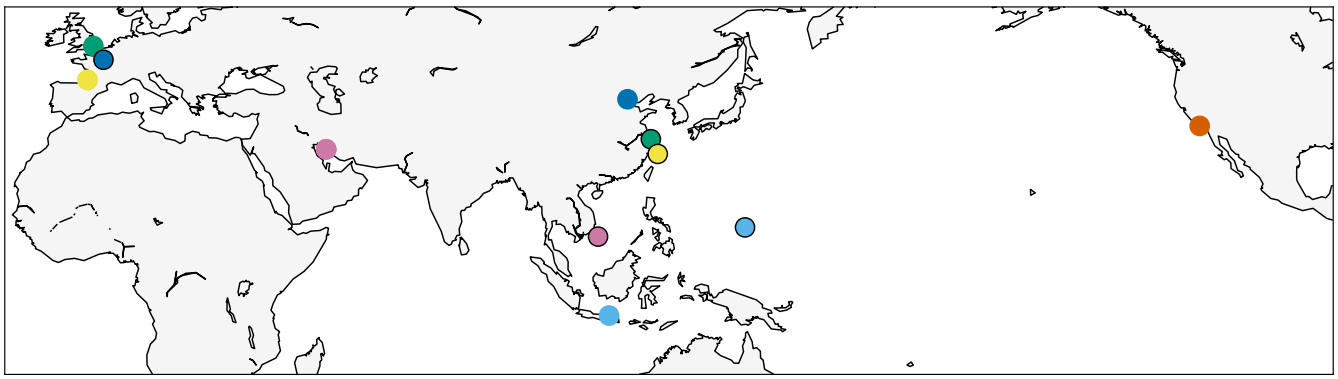

Location	Concentration (MP m^{-3})	Analytical method
Beijing, China[13]	5650	SEM-EDX
London, UK[12]	2502	Raman spectral imaging
Surabaya, Indonesia[20]	109	FTIR
Bushehr Port, Iran (dusty days)[1]	10.3	µRaman
French Atlantic Coast (offshore wind)[3]	9.6	µRaman
Southern California[9]	6.2	µRaman and µFTIR
French Atlantic Coast (onshore wind)[3]	2.9	µRaman
Bushehr Port, Iran (normal days)[1]	2.1	µRaman
Shanghai, China[14]	1.42	µFTIR
Paris, France[8]	0.9	µFTIR
East China Sea[15]	0.13	µFTIR
South China Sea and West Pacific Ocean[17]	0.11	µFTIR
West Pacific Ocean[15]	0.01	µFTIR

Fig. 1 | Concentrations of airborne microplastics reported by previous studies. All studies relied on pumped air (active) sampling rather than deposition collection (passive sampling), and all studies confirmed polymer composition spectroscopically via either FTIR, Raman or SEM-EDX spectroscopy. The mean and median concentrations are 638 and 2.9 MP m^{-3}, respectively. Map data sourced from https://www.soest.hawaii.edu/pwessel/gshhg/[47].

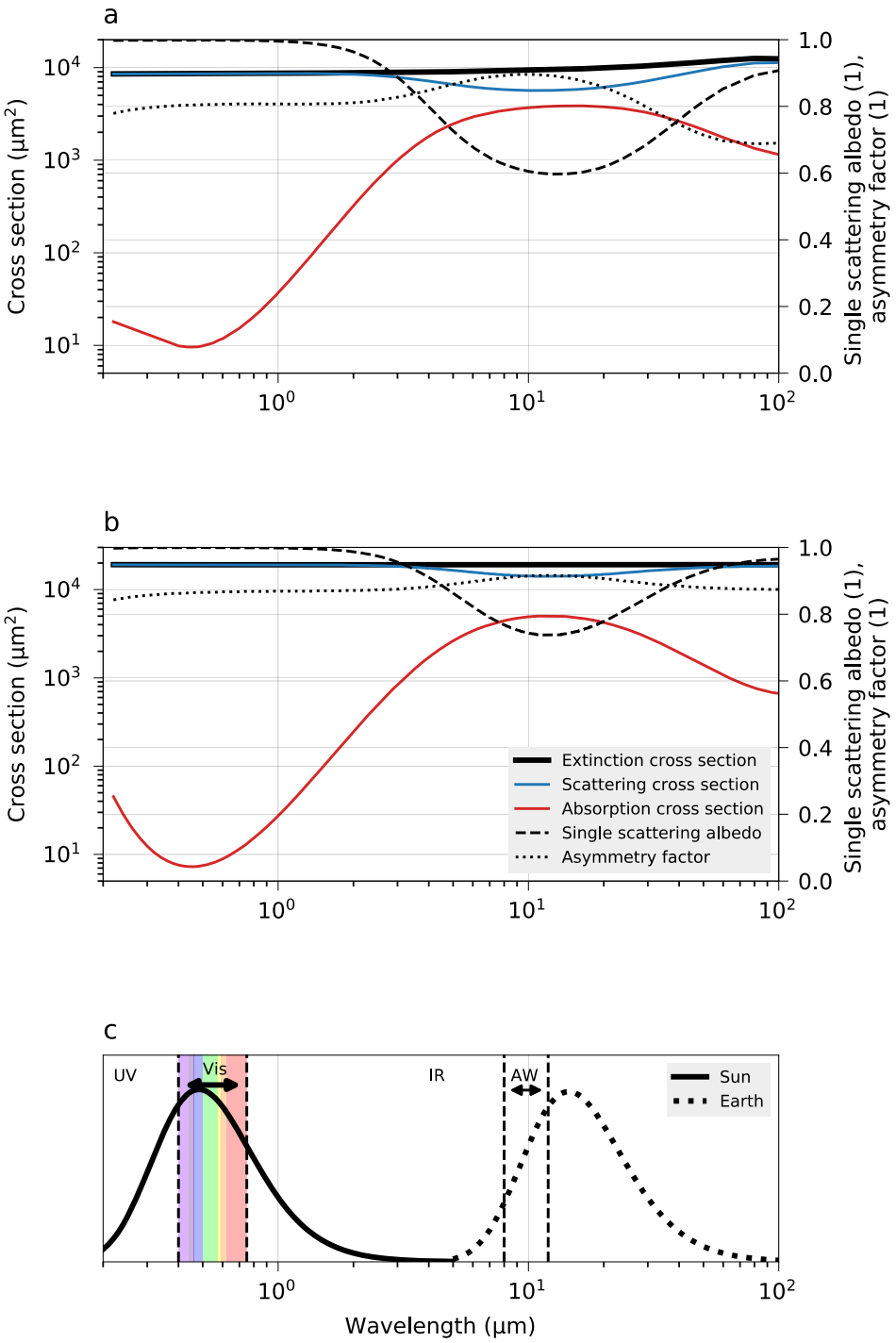

Fig. 2 | Optical properties of microplastic fragments and fibres. (a) Fragment cross sections, single scattering albedo and asymmetry factor calculated by Mie theory assuming a theoretical gamma size distribution (Extended Data Fig. 2) and an idealised refractive index (Extended Data Fig. 5). (b) As for (a) but showing optical properties for fibres calculated assuming a theoretical gamma size distribution (Extended Data Fig. 3). For reference, (c) shows the normalised intensity of blackbody radiation emitted by the Sun and Earth. 'AW' denotes the infrared atmospheric window, the region between 8 – 12 μm where relatively little absorption of terrestrial radiation by greenhouse gases occurs aside from the ozone absorption band at 9.6 μm.

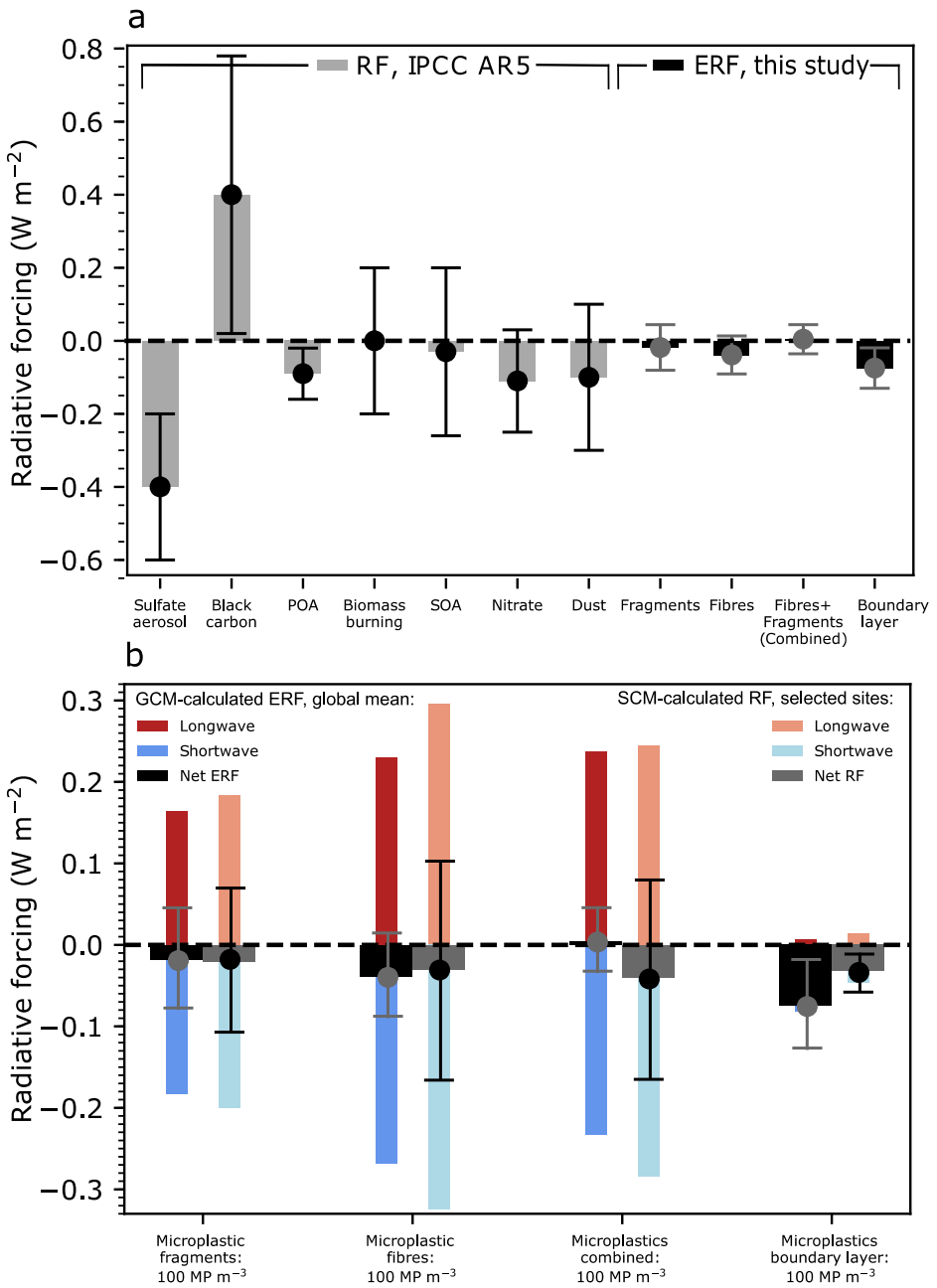

Fig. 3 | Effective radiative forcing (ERF) of airborne microplastics. (a) Global- and annual-mean clear-sky ERF values are shown for non-pigmented microplastics, averaged over 20-year GCM simulations for fragments, fibres, and a combined fragments and fibres simulation. Microplastics are assumed to be present up to 10 km with a surface concentration of 100 MP m^{-3}. Also shown is a simulation in which microplastics are assumed to be in the boundary layer only (bottom 2 km of the atmosphere), with a surface concentration of 100 MP m^{-3}. Error bars indicate the 90% confidence interval (see Methods). For comparison the global- and annual-mean radiative forcing (RF) due to aerosol-radiation interactions between 1750 and 2011 of seven aerosol components are included as listed in Table 8.4 of IPCC AR5[26]. POA represents primary organic aerosol; SOA represents secondary organic aerosol. (b) Global-, annual-mean microplastic ERF is shown for the simulations presented in (a), along with longwave and shortwave ERF. Also shown are RF values calculated from a simple set of SCM simulations using fixed temperature profiles and clouds for selected geographical sites and solar zenith angles. Error bars represent the mean plus/minus one standard deviation. Note the different y axis ranges in (a) and (b).

Methods

Empirical properties of airborne microplastics

Morphotype

Microplastics are typically categorised as fragments, fibres and films according to their morphotype. Because the shape of a particle affects how it scatters and absorbs radiation, it is important to take morphotype into account when calculating optical properties. Morphotypes reported by eight studies are summarised in Extended Data Fig. 4. For simplicity, granules were included in the same group as fragments. The median occurrence of fibres, fragments and films was approximately 60%, 35% and 20%, respectively (not normalised to unity). Since films are less common than other morphotypes and little is known about their size distribution to date, they were excluded from further analysis. In carrying out our first assessment of the combined ERF of microplastic fragments and fibres, we approximated their median occurrences to assume a combination of 50% fragments and 50% fibres (Extended Data Table 1).

Size distribution and aspect ratio

Size distributions of airborne microplastic fibres and fragments are approximated by gamma distributions in Extended Data Fig. 2, 3. Fragment diameters peak at approximately 10 μm while fibre lengths peak at approximately 200 μm. Fibres are characterised by their length and diameter. In reality they also occur in curved shapes, but considering the uncertainties involved in our other assumptions, we do not expect this to be a limiting factor in the accuracy of the ERF calculations. Extended Data Fig. 7 shows the empirical aspect ratio of fibres[4]. To simplify the result we approximated the relationship between the fibre length L and diameter D by fitting a logarithmic curve of the form:

$$D = A \log\left(1 + \frac{L}{B}\right) \tag{1}$$

where A = 6 μm and B = 30 μm are coefficients determined using the least squares method, and rounded to the nearest integer.

Refractive index

The optical properties of materials depend on the (dimensionless) refractive index as a function of wavelength. Refractive indices of pure polymers are shown in Extended Data Fig. 5[48-54]. Due to the similarities in the wavelength-dependent refractive index of different polymers and the lack of data for all polymer types, we approximated the refractive index of airborne microplastics with an empirical, analytical, average form. For the real part, n, (responsible for refraction) we used a one-term Sellmeier model[55]:

$$n = \left(1 + \frac{a\lambda^2}{\lambda^2 - b^2}\right)^{\frac{1}{2}} \tag{2}$$

where λ is the wavelength and a and b are determined by least squares optimisation. The coefficients were determined as a = 1.4 and b = 1.1 ×10^{-7} m. For the imaginary part k (which determines the absorption coefficient), we fitted a fourth degree polynomial by least squares optimisation between 0.4 μm and 100 μm:

$$\log_{10}(k) = c_0 + c_1 x + c_2 x^2 + c_3 x^3 + c_4 x^4 \tag{3}$$

x is the $\log_{10}$ of the wavelength in m, and the coefficients were determined as c_0 = 550, c_1 = 460, c_2 = 140, c_3 = 19, c_4 = 0.93. As k is much smaller than n, this polynomial approximation remains compatible with the Kramers-Krönig relations.

Colour and composition

Due to the lack of measurements of optical properties of coloured plastics, we did not account for different colours in our refractive index models. Future research should assess the impact of colour on microplastic ERF and we therefore include colour and composition information here for completeness. The colour of atmospheric microplastics based on six studies is summarised in Extended Data Fig. 6. The most commonly reported colour was black (including grey; median occurrence 30%) followed by red (median occurrence 23%), white (including transparent), yellow and blue (median occurrence ~12% each).

Microplastics can be broadly characterised as synthetic, such as polyethylene and polypropylene, or semi-synthetic such as rayon, viscose or cellophane[56]. Here we assess the impact of synthetic microplastics which are generally non-biodegradable (unlike semi-synthetic plastics) and therefore more likely to be widespread in the environment. Previous studies reported a mixture of synthetic, semi-synthetic and natural fibres since natural fibres may contain toxic dyes which could yield similar harmful effects on the environment as synthetic fibres[6,7]. Extended Data Figs. 1, 2 show the composition of environmental fragments and fibres. Fragments were mostly resins and polyethylene and polypropylene (median occurrence ~25% each). Fibres were predominantly polyester (median occurrence 80%), likely originating from synthetic textiles, followed by polyethylene and polypropylene (median occurrence 20%), with a smaller contribution of acrylic, polyamide (including nylon) and polyurethane (median occurrence ~10% each). The reported microplastic compositions compare reasonably well with the production data reported for the European and Asian markets, which is where the majority of studies summarised in Fig. 1 were performed. In Europe and Asia, the most commonly produced polymers are polypropylene, polyethylene and polyvinyl chloride[57,58].

Calculation of microplastic optical properties

Fragments

We assumed that fragments are approximately spherical and calculated their scattering and absorption efficiencies and asymmetry factors using Mie theory. Calculations were performed with the Suite of Community Radiative Transfer codes based on Edwards and Slingo (SOCRATES)[59]. Mie scattering and absorption cross sections, single-scattering albedos and asymmetry factors of spherical fragments calculated with a fitted refractive index and assuming a gamma size distribution are shown in Fig. 2. The optical parameters were weighted by the incoming solar spectrum[60] to calculate integral properties in each spectral band. The integral properties were then used to prepare volume scattering and absorption coefficients and asymmetry factors for the GCM by multiplying by the number concentration (in MP m^{-3}) of fragments (Extended Data Table 2).

Fibres

We assumed that the fibres' lengths were distributed as a gamma distribution with a shape parameter of 2.5, and a scale parameter of 250 μm as in Extended Data Fig. 3, for lengths L from 10 to 2500 μm. The diameter D of the fibres was assumed to follow Eq. 1. Fibres were considered to be cylinders of length $L - D$, with a hemispherical cap at each end to give a total length of L. Because fibres have typically large size parameters $L/\lambda \gg 1$, we used a combination of geometric ray-tracing and the extinction paradox to estimate the scattering properties[61]. This gives the orientation-averaged extinction cross section as $\langle C_{ext} \rangle = S/2$, where S is the surface area[62]. The absorption cross section is estimated by the method of Kokhanovsky and Macke[63], which itself is an extension of Bohren and Huffman[64]. This expresses the orientation-averaged absorption cross section as:

$$\langle C_{\mathrm{abs}} \rangle = \frac{S}{4}\left[1 - R(n)\right]\left[1 - \mathrm{e}^{-\psi(n)c(k)}\right] \tag{4}$$

where $R(n)$ is the reflectance of Lambertian light from an interface[65], $\psi(n)=\frac{2\phi(n)}{3(1-R(n))}$, $\phi(n)$ is the mean path length of rays incident on the object, and $c(k)=3\alpha(k)/(2S)$ for a fibre with volume V and surface area S, and $\alpha(k)=4\pi k/\lambda$ is the absorption coefficient. Ray-tracing simulations were used to obtain $\phi(n)$. The orientation-averaged scattering cross section is then obtained as $\langle C_{sca}\rangle=\langle C_{ext}\rangle-\langle C_{\mathrm{abs}}\rangle$.

The asymmetry factor g is obtained following Kokhanovsky and Macke[63] as:

$$g=g_{\infty}(n)-\left[g_{\infty}(n)-g_0(n)\right]\exp\left(-\beta(n)c(k)\right) \tag{5}$$

$c(k)$ was defined earlier and is the only parameter depending on the absorption coefficient (but not on n). g_{∞} is the asymmetry factor at high absorption – it depends on the refractive index n but is independent of shape for randomly oriented objects and therefore we can use the known analytic expression for a sphere[61]. $g_0$is the asymmetry factor at zero absorption and depends on the shape (but not size) and refractive index of the object. We calculate it from ray-tracing simulations. $\beta(n)$ also depends on the shape (not size) and n. For a given shape and n, we can derive β by calculating g in a single ray-tracing simulation in the low-absorbing case (we used $c(k)=3.75\times10^{-4}$) and inverting Eq. 5 in this limit:

$$\beta\equiv\frac{g-g_0}{\left(g_{\infty}(n)-g_0\right)c} \tag{6}$$

The properties that are extracted from ray tracing (g_0 and β) were calculated on a grid of seven linearly spaced refractive indices from 1.5 to 1.8, and 50 shapes with aspect ratios from 1 to 200, spaced on a log-scale. Values used in the calculations were then linearly interpolated from these data. The ray-tracing simulations used 10^7 rays incident on each object.

As was done for fragments, fibre optical parameters were weighted by the incoming solar spectrum[60] to calculate integral properties in each spectral band. These were then used to prepare volume-scattering and absorption coefficients and asymmetry factors as an input to the GCM by multiplying by the number concentration of fibres. Extended Data Table 2 contains the fibre optical properties input to the GCM.

Modelling direct radiative effects

HadGEM3 general circulation model

To assess the effect of airborne microplastics on the global energy balance, we performed simulations with the Hadley Centre Global Environment Model version 3 – Global Atmosphere model 7.1 (HadGEM3-GA7.1)[66], developed by the UK Met Office and the Unified Model Partnership. The model uses a regular longitude – latitude 1.875° × 1.25° grid with 85 vertical levels between the surface and 85 km, and the radiative transfer scheme SOCRATES[59]. The radiative transfer scheme divides the shortwave part of the spectrum between 200 nm and 10 μm into six spectral bands and the longwave part between 3.3 μm and 1 cm into nine spectral bands.

We used HadGEM3's EasyAerosol scheme[67] to supply the radiative transfer code with a 5-dimensional (longitude × latitude × level × spectral band × time) grid of volume scattering and absorption coefficients and asymmetry factors calculated for the given concentration and optical properties of microplastics. The absorption and scattering coefficients of microplastics were added to the model's coefficients calculated for atmospheric gases, aerosols and clouds. We considered only direct aerosol-radiation interactions in calculating microplastic ERF, since little is known to date regarding whether microplastics play a role in indirect aerosol effects on cloud lifetime and albedo.

Due to the current lack of globally distributed and vertically resolved measurements, we assume that airborne microplastics are distributed uniformly over the Earth. While previous studies indicate that the distribution is not uniform (Fig. 1), too few measurements are available to date – particularly from the Southern Hemisphere

– to derive a global distribution. Prescribing a uniform concentration allows us to obtain a conservative first estimate of microplastic ERF.

Aside from a recent series of aircraft flights that identified microplastic concentrations of up to 20 MP m^{-3} above the planetary boundary layer[36], little is known about the vertical distribution of microplastic, including the maximum altitude at which they may be found. We have assumed that microplastics are most abundant at the surface and that their concentration decreases with altitude. We prescribed a vertical distribution of microplastics in the model assuming that the concentration decreases to 0.3 of the surface concentration at 10 km above sea level, since air density at 10 km is approximately 0.3 of the surface air density. The vertical distribution of microplastics was calculated as:

$$[MP]_z = 0.3^{\frac{z}{10}} \quad (7)$$

where z is the altitude in km above sea level and $[MP]_z$ is the microplastic concentration at that altitude. We assumed that microplastics are not transported into the stratosphere, and thus set the microplastic concentration above 10 km (the approximate height of the tropopause) to zero.

To test our assumptions regarding vertical distribution, we performed a sensitivity simulation in which microplastics were confined to the lowest 2 km of the atmosphere (the approximate height of the boundary layer). The vertical distribution was computed using Eq. (7), and the microplastic concentration above 2 km was set to zero.

Simulations and calculation of ERF

Five simulations were performed, each of 20 years' duration from 1990 – 2009 (Extended Data Table 1). Sea surface temperatures, sea ice concentrations and greenhouse gas concentrations were prescribed based on observations and aerosol emissions were taken from the CMIP5 database[68]. Microplastic surface concentrations were prescribed as in Extended Data Table 1, i.e. with 100× scaling applied. This was done to clearly isolate signal from noise, under the assumption that ERF scales linearly with concentration. ERF is defined here as the difference in the global-mean net top-of-atmosphere radiation flux between simulations with and without microplastics[69].

We derived confidence intervals for the net ERF as follows. We calculated $N = 20$ annual geographical means from daily mean values of the top-of-atmosphere flux for the experimental and control runs, resulting in two vectors X_{exp} and X_{cnt} of length N, respectively. The geographical mean was weighted by the surface area of grid cells. We assumed that the annual means are approximately statistically independent between years and normally distributed. Next, we calculated the difference between the experimental and control run, $X = X_{exp} - X_{cnt}$. From these 20 X values, we calculated the mean $\acute{X}$ and standard deviation s. The distribution of the long-term (20-year) difference between the experimental and control run is then t-distributed with $N - 1$ degrees of freedom, a shift of $\acute{X}$ and scale of $s/\sqrt{N}$. Lastly, we calculated the 90% confidence interval as the 5th to 95th percentiles of this t-distribution.

Single column modelling

To assess the effect of atmospheric microplastics on radiative transfer, ignoring rapid adjustments induced by microplastics (for example, changes in clouds), we performed simulations with a single column model (SCM). We applied the radiative transfer code SOCRATES on the Continual Intercomparison of Radiation Codes (CIRC) cases[70], which provide thermodynamic, cloud and aerosol profiles based on observations along with reference measured and calculated radiative fluxes. The SCM consisted of only the radiative transfer code and did not simulate dynamics or physics. Holding atmospheric temperature, pressure and composition profiles, surface temperature, albedo and clouds fixed in the SCM allowed us to quantify the radiative effect of microplastics in these simple scenarios without rapid adjustments. We ran the SOCRATES code with the

unmodified CIRC profiles (control simulations). For each CIRC case, we also ran the code with prescribed microplastics as in the GCM simulations (i.e., with a surface concentration of 100 MP m^{-3} and vertical scaling applied; Extended Data Table 1). Radiative flux differences were calculated for each simulation relative to the control simulation.

Methods references

48 Horwitz, J. W. Infrared refractive index of polyethylene and a polyethylene-based material. *Optical Engineering* **50**, 1-5, doi:10.1117/1.3615652 (2011).

49 Smith, D. R. & Loewenstein, E. V. Optical constants of far infrared materials. 3: plastics. *Appl. Opt.* **14**, 1335-1341, doi:10.1364/AO.14.001335 (1975).

50 Sultanova, N., Kasarova, S. & Nikolov, I. Dispersion Properties of Optical Polymers. *Acta Physica Polonica A* **116**, 585-587, doi:10.12693/aphyspola.116.585 (2009).

51 Zhang, X., Qiu, J., Zhao, J., Li, X. & Liu, L. Complex refractive indices measurements of polymers in infrared bands. *Journal of Quantitative Spectroscopy and Radiative Transfer* **252**, 107063, doi:10.1016/j.jqsrt.2020.107063 (2020).

52 Zhang, X., Qiu, J., Li, X., Zhao, J. & Liu, L. Complex refractive indices measurements of polymers in visible and near-infrared bands. *Appl. Opt.* **59**, 2337-2344, doi:10.1364/AO.383831 (2020).

53 Flores-Mijangos, J. & Beltrán-López, V. Far-infrared laser measurement of the refractive index of polypropylene. *Appl. Opt.* **42**, 592-596, doi:10.1364/AO.42.000592 (2003).

54 Myers, T. L. *et al.* Accurate Measurement of the Optical Constants n and k for a Series of 57 Inorganic and Organic Liquids for Optical Modeling and Detection. *Applied Spectroscopy* **72**, 535-550, doi:10.1177/0003702817742848 (2017).

55 Sellmeier, W. Ueber die durch die Aetherschwingungen erregten Mitschwingungen der Körpertheilchen und deren Rückwirkung auf die ersteren, besonders zur Erklärung der Dispersion und ihrer Anomalien. *Annalen der Physik* **223**, 386-403, doi:10.1002/andp.18722231105 (1872).

56 Kroon, F. J., Motti, C. E., Jensen, L. H. & Berry, K. L. E. Classification of marine microdebris: A review and case study on fish from the Great Barrier Reef, Australia. *Scientific Reports* **8**, 16422, doi:10.1038/s41598-018-34590-6 (2018).

57 PlasticsEurope. *Plastics – the Facts 2018: An analysis of European plastics production, demand and waste data*, http://www.plasticseurope.org (2018). Last access: 03/05/2021.

58 Plastemart. *China leads in growth of polymers & plastic products*, www.plastemart.com/upload/Literature/chineseplasticandpolymergrowth.asp. Last access: 03/05/2021.

59 Edwards, J. M. & Slingo, A. Studies with a flexible new radiation code. I: Choosing a configuration for a large-scale model. *Quarterly Journal of the Royal Meteorological Society* **122**, 689-719, doi:10.1002/qj.49712253107 (1996).

60 Lean, J. L. & DeLand, M. T. How Does the Sun's Spectrum Vary? *Journal of Climate* **25**, 2555-2560, doi:10.1175/JCLI-D-11-00571.1 (2012).

61 Kokhanovsky, A. A. & Zege, E. P. Local optical parameters of spherical polydispersions: simple approximations. *Appl. Opt.* **34**, 5513-5519, doi:10.1364/AO.34.005513 (1995).

62 van de Hulst, H. C. *Light scattering by small particles*. (Wiley, 1957).

63 Kokhanovsky, A. A. & Macke, A. Integral light-scattering and absorption characteristics of large, nonspherical particles. *Appl. Opt.* **36**, 8785-8790, doi:10.1364/AO.36.008785 (1997).

64 Bohren, C. F. & Huffman, D. R. *Absorption and scattering of light by small particles*. (John Wiley & Sons Inc., 1983).

65 Duntley, S. Q. The Optical Properties of Diffusing Materials. *J. Opt. Soc. Am.* **32**, 61-70, doi:10.1364/JOSA.32.000061 (1942).

66 Walters, D. *et al.* The Met Office Unified Model Global Atmosphere 7.0/7.1 and JULES Global Land 7.0 configurations. *Geosci. Model Dev.* **12**, 1909-1963, doi:10.5194/gmd-12-1909-2019 (2019).

67 Edwards, J. M., Manners, J., Thelen, J.-C., Ingram, W. J. & Hill, P. G. Unified Model Documentation Paper 023: The Radiation Code (UM Version 11.4). (Met Office, Exeter, United Kingdom, 2018).

68 Lamarque, J. F. *et al.* Historical (1850–2000) gridded anthropogenic and biomass burning emissions of reactive gases and aerosols: methodology and application. *Atmos. Chem. Phys.* **10**, 7017-7039, doi:10.5194/acp-10-7017-2010 (2010).

69 Forster, P. M. *et al.* Recommendations for diagnosing effective radiative forcing from climate models for CMIP6. *Journal of Geophysical Research: Atmospheres* **121**, 12, 460-412, 475, doi:10.1002/2016jd025320 (2016).

70 Oreopoulos, L., & Mlawer, E. Modeling: The Continual Intercomparison of Radiation Codes (CIRC). *Bulletin of the American Meteorological Society* **91** 3, 305-310, doi: 10.1175/2009BAMS2732.1 (2010).

Data availability

GCM data that support the findings of this study are available at https://doi.org/10.5281/zenodo.5093843.

Code availability

Custom code generated in this study is available at https://doi.org/10.5281/zenodo.5093843.

Acknowledgements

This research was supported by the Royal Society of New Zealand Marsden Fund (Contract MFP-UOC1903). The authors acknowledge the UK Met Office for the use of the MetUM, SOCRATES and the Continual Intercomparison of Radiation Codes (CIRC). The authors acknowledge the contribution of New Zealand eScience Infrastructure (NeSI) high-performance computing facilities to the results of this research. New Zealand's national facilities are provided by NeSI and funded jointly by NeSI's collaborator institutions and through the Ministry of Business, Innovation and Employment's Research Infrastructure programme (https://www.nesi.org.nz, last access: 20 April 2021). The authors also acknowledge the use of the Rāpoi computing facility at Victoria University of Wellington, along with the open source software used in the analysis: Devuan GNU+Linux, Python, numpy, scipy and matplotlib. LER thanks Jonny Williams for technical assistance. LER and PK acknowledge Rodrigo Martinez Gazoni for helpful discussions. The authors thank Ben Booth, Steve Allen and the other anonymous reviewers for helpful suggestions and comments.

Author contributions

LER: Conceptualization, Formal analysis, Writing – original draft, Visualization, Supervision, Funding acquisition. PK: Methodology, Software, Validation, Formal analysis, Writing – original draft. ECL: Methodology, Validation, Writing – review & editing, Supervision, Funding acquisition. WRCS: Software, Validation, Formal analysis, Writing – original draft. SKG: Writing – review & editing, Funding acquisition.

Additional information

The authors declare no competing interests. Extended Data are available for this paper. Correspondence and requests for materials should be addressed to Laura Revell (laura.revell@canterbury.ac.nz).

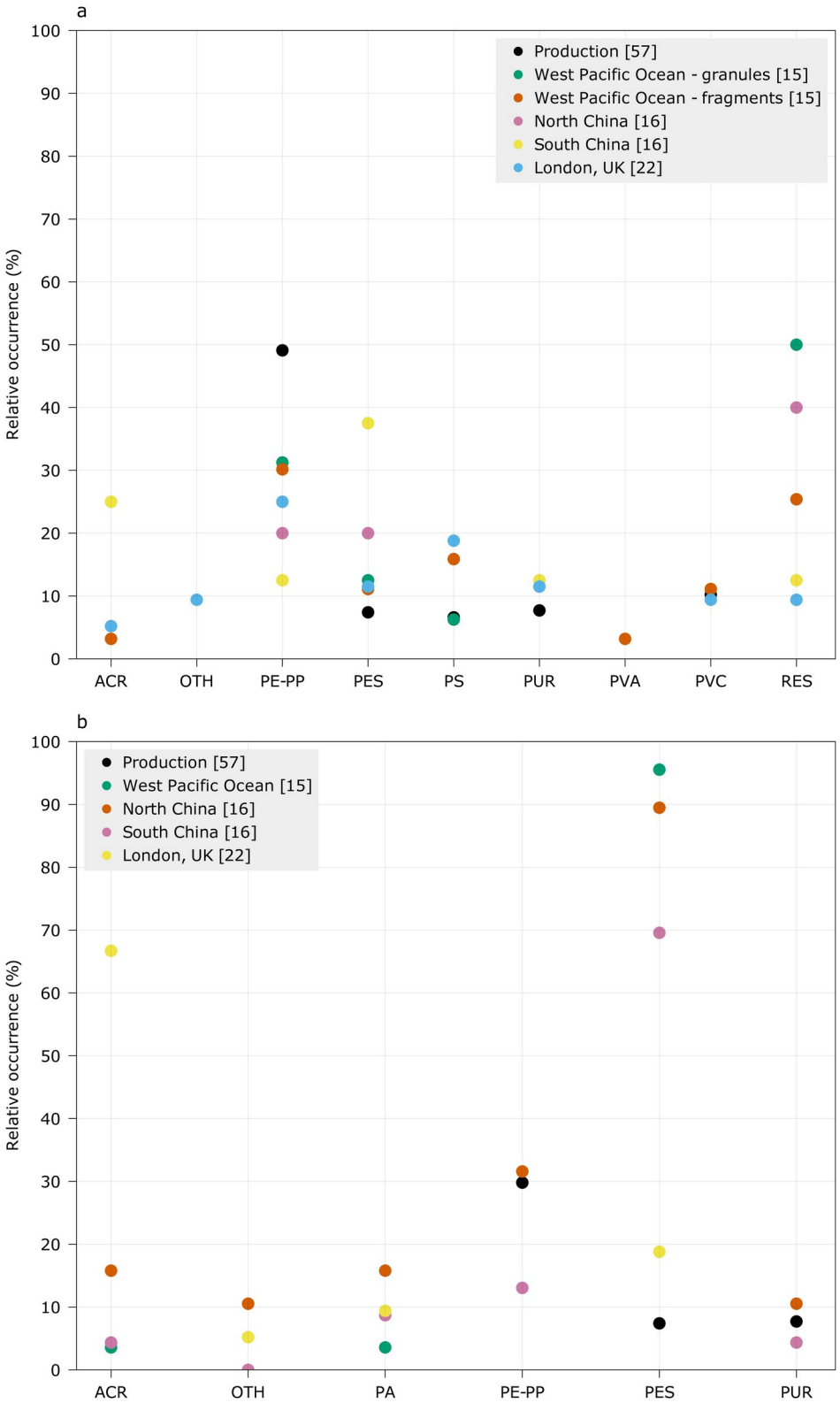

Extended Data Fig. 1 | Composition of airborne microplastics collected in previous studies compared with reported plastic production data. The studies included disaggregated composition by morphotype and are presented for (a) fragments; (b) fibres. Polymer compositions include acrylic (ACR, including polyacrylonitrile and poly(N-methyl acrylamide)), polyamide (PA, including nylon), polyethylene and polypropylene (PE-PP), polyester (PES, including polyethylene terephthalate), polystyrene (PS), polyurethane (PUR), polyvinyl acetate (PVA), polyvinyl chloride (PVC), resins (RES, including epoxy, phenoxy and alkyd resins), and various other types (OTH).

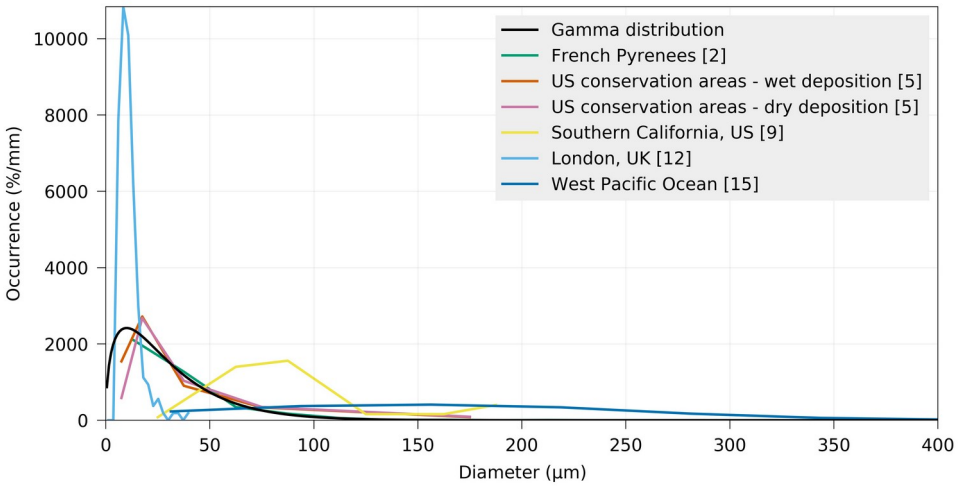

Extended Data Fig. 2 | Size distributions of microplastic fragments reported by previous studies. A gamma distribution was fitted to match the majority of the empirical distributions. The distributions are normalised to unity and approximated by a gamma distribution with the shape parameter of 2 and scale parameter 15 μm.

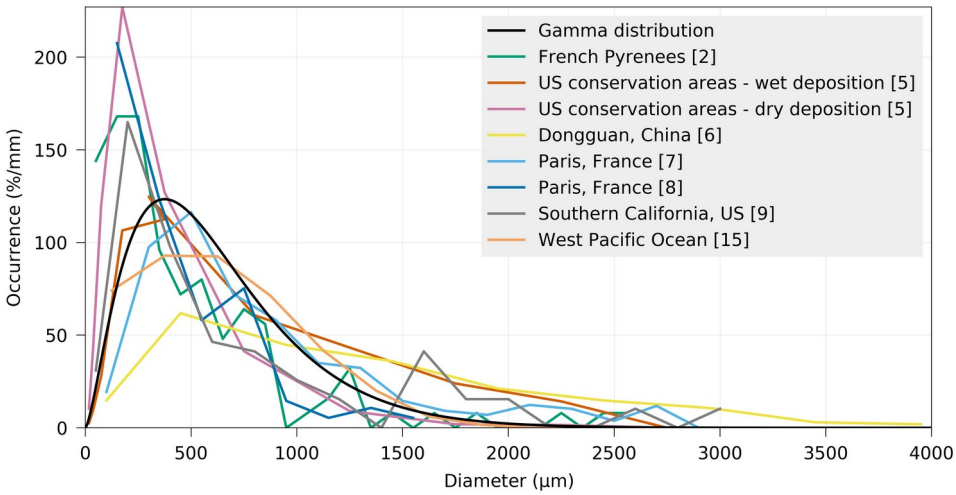

Extended Data Fig. 3 | Size distributions of microplastic fibre lengths reported by previous studies. A gamma distribution was fitted to match the majority of the empirical distributions. The distributions are normalised to unity and approximated by a gamma distribution with the shape parameter of 2.5 and scale parameter 250 μm.

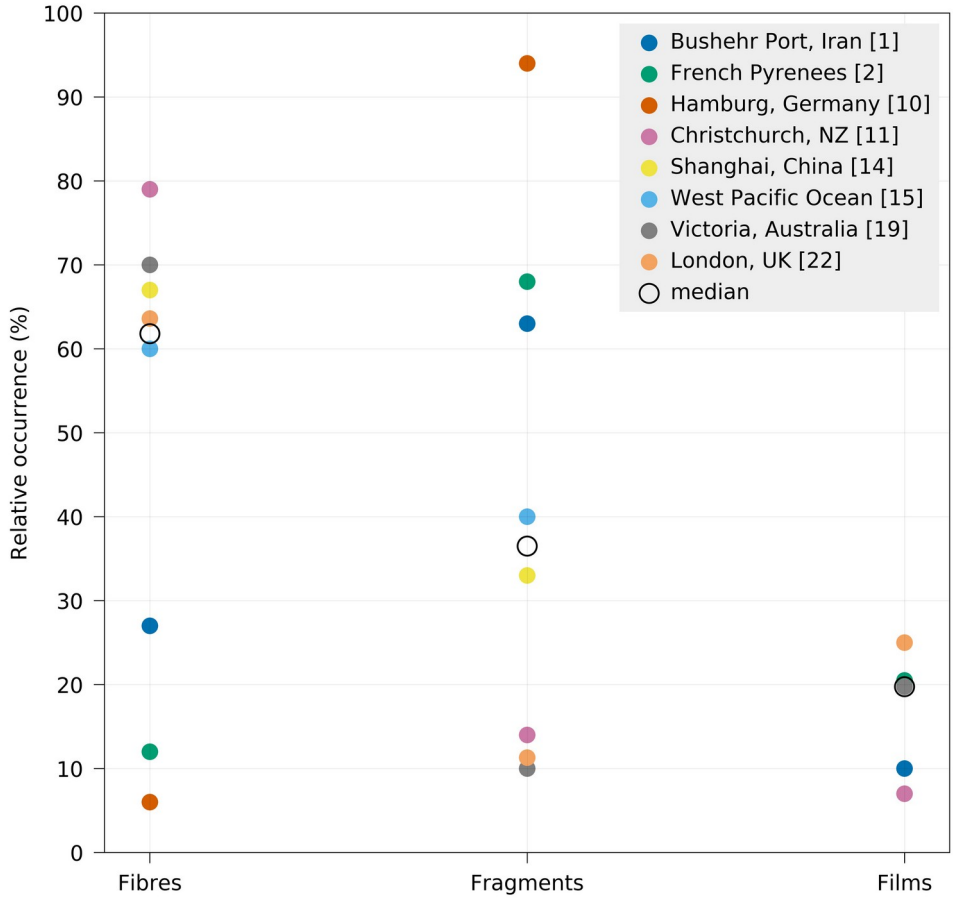

Extended Data Fig. 4 | Morphotypes of airborne microplastic collected in previous studies.

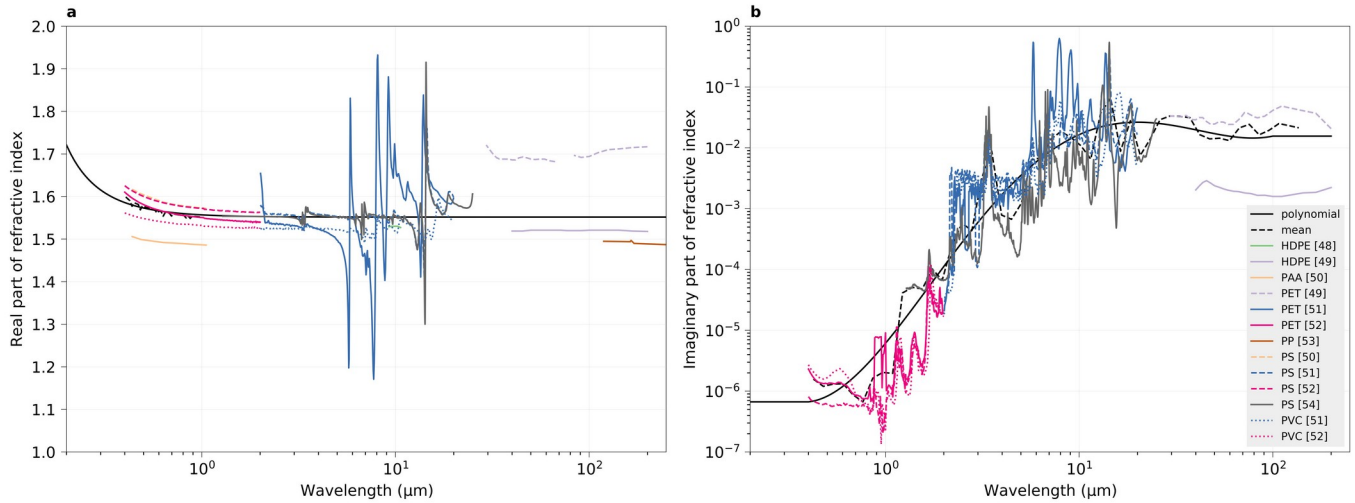

Extended Data Fig. 5 | Refractive index of polymers based on a literature survey. Polymer compositions include high-density polyethylene (HDPE), polyacrylic acid (PAA), polyethylene terephthalate (PET), polypropylene (PP), polystyrene (PS) and polyvinyl chloride (PVC). The mean calculated over regular wavelength intervals on a $\log_{10}$ scale is shown by the dashed black lines. In (a) Equation 2 was fitted to the mean. In (b) Equation 3 was used to fit a 4^{th} degree polynomial to the $\log_{10}$ of the mean using the least squares method. The solid black lines represent the fits given by Equations 2 and 3, and these fits were used in the calculations of microplastic optical properties.

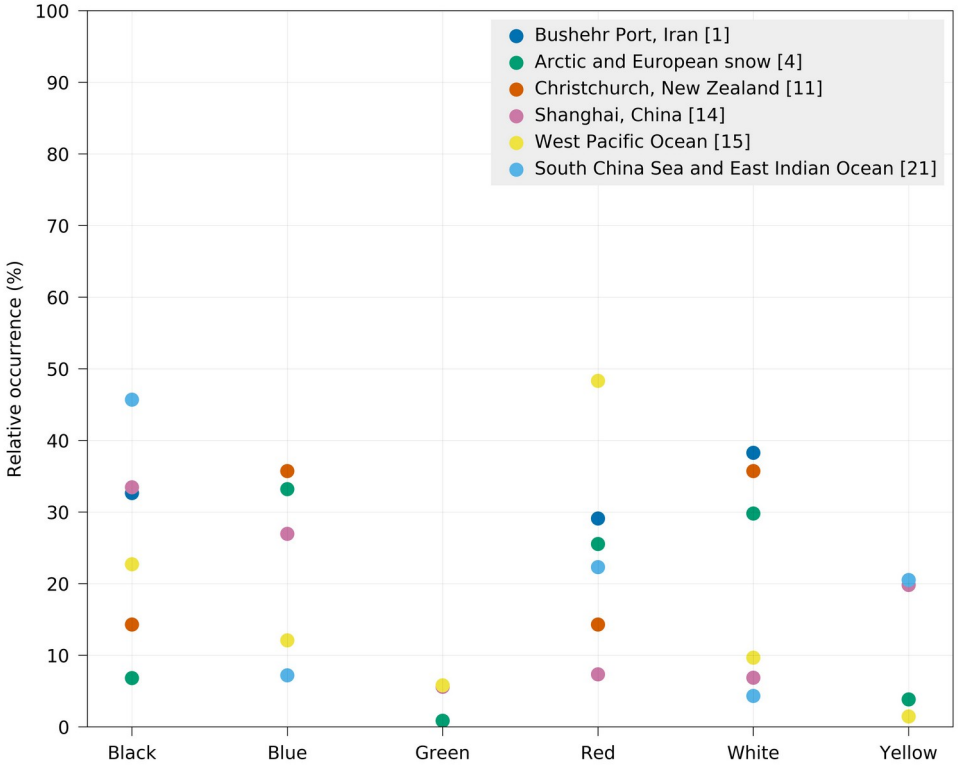

Extended Data Fig. 6 | Colours of airborne microplastics collected in previous studies, where colour was reported. Black includes grey; blue includes turquoise; green includes lime; red includes pink, purple, brown and orange; white includes transparent.

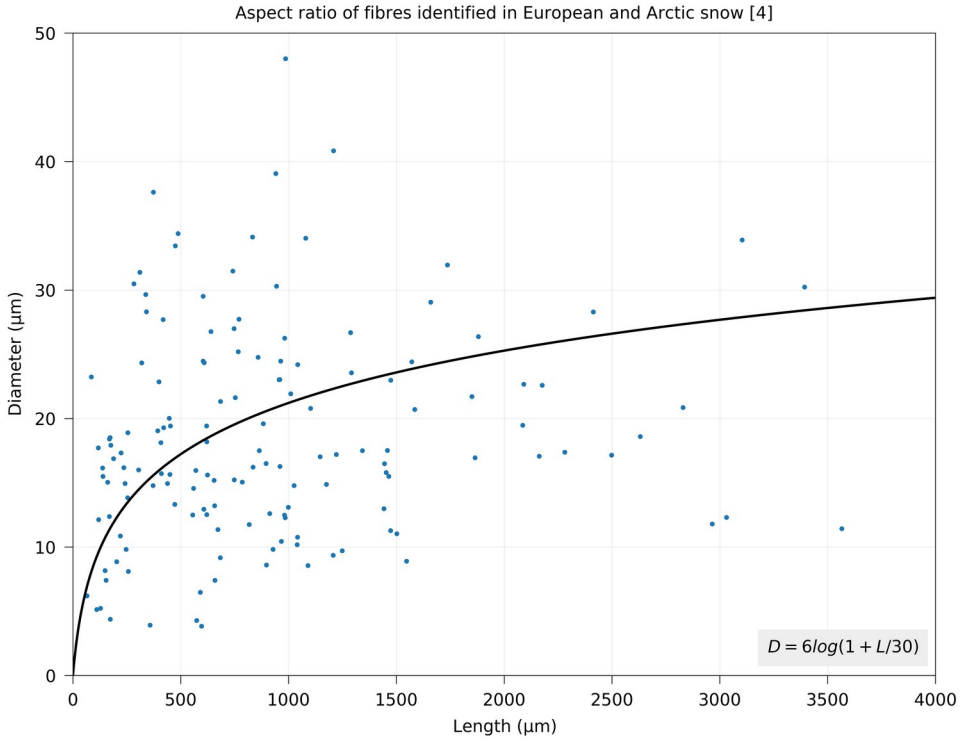

Extended Data Fig. 7 | The empirical aspect ratio of fibres collected in European and Arctic snow (the only study to date to report fibre aspect ratio). A least squares fit of the form $D = A \log\left(1 + \frac{L}{B}\right)$ is also shown, where D is the fibre diameter, L is the fibre length and A and B are fitted coefficients, rounded to the nearest integer.

Extended Data Table 1 | Prescribed microplastic surface concentrations in GCM simulations.

Experiment name	Fragments ($MP\ m^{-3}$)	Fibres ($MP\ m^{-3}$)	Altitude range (km)
Control	0	0	-
Fragments	100	0	0 – 10
Fibres	0	100	0 – 10
Combined	50	50	0 – 10
Boundary layer	50	50	0 – 2

Extended Data Table 2 | Optical properties of microplastic fragments and fibres supplied to the GCM in the shortwave and longwave bands.

Shortwave			Fragments			Fibres		
Band	Lower wavelength limit (m)	Upper wavelength limit (m)	Absorption coefficient (m^{-1})	Scattering coefficient (m^{-1})	Asymmetry factor	Absorption coefficient (m^{-1})	Scattering coefficient (m^{-1})	Asymmetry factor
1	2.00×10^{-7}	3.20×10^{-7}	1.34×10^{-11}	8.55×10^{-9}	7.95×10^{-1}	1.47×10^{-11}	1.91×10^{-8}	8.56×10^{-1}
2	3.20×10^{-7}	5.05×10^{-7}	1.01×10^{-11}	8.58×10^{-9}	8.03×10^{-1}	7.72×10^{-12}	1.91×10^{-8}	8.63×10^{-1}
3	5.05×10^{-7}	6.90×10^{-7}	1.19×10^{-11}	8.60×10^{-9}	8.07×10^{-1}	8.94×10^{-12}	1.91×10^{-8}	8.66×10^{-1}
4	6.90×10^{-7}	1.19×10^{-6}	2.95×10^{-11}	8.63×10^{-9}	8.07×10^{-1}	2.19×10^{-11}	1.91×10^{-8}	8.68×10^{-1}
5	1.19×10^{-6}	2.38×10^{-6}	1.75×10^{-10}	8.56×10^{-9}	8.09×10^{-1}	1.32×10^{-10}	1.90×10^{-8}	8.70×10^{-1}
6	2.38×10^{-6}	1.00×10^{-5}	1.30×10^{-9}	7.61×10^{-9}	8.34×10^{-1}	1.27×10^{-9}	1.79×10^{-8}	8.78×10^{-1}
Longwave			Fragments			Fibres		
Band	Lower wavelength limit (m)	Upper wavelength limit (m)	Absorption coefficient (m^{-1})	Scattering coefficient (m^{-1})	Asymmetry factor	Absorption coefficient (m^{-1})	Scattering coefficient (m^{-1})	Asymmetry factor
1	2.50×10^{-5}	1.00×10^{-2}	2.95×10^{-9}	7.75×10^{-9}	7.71×10^{-1}	2.51×10^{-9}	1.66×10^{-8}	8.89×10^{-1}
2	1.82×10^{-5}	2.50×10^{-5}	3.73×10^{-9}	6.22×10^{-9}	8.52×10^{-1}	4.11×10^{-9}	1.50×10^{-8}	9.05×10^{-1}
3	1.25×10^{-5}	1.82×10^{-5}	3.85×10^{-9}	5.77×10^{-9}	8.84×10^{-1}	4.88×10^{-9}	1.43×10^{-8}	9.14×10^{-1}
4	1.33×10^{-5}	1.69×10^{-5}	3.86×10^{-9}	5.77×10^{-9}	8.84×10^{-1}	4.88×10^{-9}	1.43×10^{-8}	9.14×10^{-1}
5	8.33×10^{-6}	1.25×10^{-5}	3.66×10^{-9}	5.69×10^{-9}	8.95×10^{-1}	4.84×10^{-9}	1.43×10^{-8}	9.14×10^{-1}
6	8.93×10^{-6}	1.01×10^{-5}	3.64×10^{-9}	5.68×10^{-9}	8.96×10^{-1}	4.82×10^{-9}	1.43×10^{-8}	9.13×10^{-1}
7	7.52×10^{-6}	8.33×10^{-6}	3.43×10^{-9}	5.80×10^{-9}	8.93×10^{-1}	4.40×10^{-9}	1.47×10^{-8}	9.08×10^{-1}
8	6.67×10^{-6}	7.52×10^{-6}	3.25×10^{-9}	5.92×10^{-9}	8.89×10^{-1}	4.04×10^{-9}	1.51×10^{-8}	9.04×10^{-1}
9	3.34×10^{-6}	6.67×10^{-6}	1.96×10^{-9}	7.01×10^{-9}	8.52×10^{-1}	1.97×10^{-9}	1.72×10^{-8}	8.84×10^{-1}